



Power Electronic Systems  
Laboratory

© 2021 IEEE

Proceedings of the 13th International Symposium on Linear Drives for Industry Application (LDIA2021), Wuhan, China,  
July 1-4, 2021

## **Control System Design and Experimental Verification of a Self-Bearing Double-Stator Linear-Rotary Actuator**

R. Giuffrida,  
S. Miric,  
A. Horat,  
D. Bortis,  
J. W. Kolar

Personal use of this material is permitted. Permission from IEEE must be obtained for all other uses, in any current or future media, including reprinting/republishing this material for advertising or promotional purposes, creating new collective works, for resale or redistribution to servers or lists, or reuse of any copyrighted component of this work in other works.



Eidgenössische Technische Hochschule Zürich  
Swiss Federal Institute of Technology Zurich

# Control System Design and Experimental Verification of a Self-Bearing Double-Stator Linear-Rotary Actuator

Rosario V. Giuffrida, Spasoje Mirić, Andreas Horat, Dominik Bortis and Johann W. Kolar

Power Electronic Systems Laboratory, ETH Zurich, Zurich, Switzerland  
giuffrida@lem.ee.ethz.ch

**Abstract**—Integrated Linear Rotary Actuators (LiRAs) offer a compact solution which can achieve high dynamics when coupled linear and rotary motions are required. As a further step in integration, the LiRA can be equipped with Active Magnetic Bearings, which however requires a special winding configuration and feedback control of the magnetically levitated mover’s position to operate. In this paper a control-oriented analysis of a Self-Bearing (SB) Double-Stator (DS) LiRA is conducted, providing an insight on simultaneous bearing force and torque generation and deriving an electromechanical dynamic model which is linearized and used to design a 6-DoF cascaded position control system. This is then implemented in hardware and verified, bringing a prototype of the SB DS LiRA into full operation, tracking a linear-rotary mission profile with radial deviations of the levitated mover’s position below 75 $\mu$ m.

## I. INTRODUCTION

Linear Rotary Actuators (LiRAs) are employed in applications which require coupled linear and rotary motion, like e.g. pick-and-place robots [1], tooling machines or gearboxes [2]. The simplest way of obtaining a LiRA is the mechanical coupling of two independent actuators together. A more compact, integrated solution is to enable linear and rotary motion in the same functional volume electromagnetically, obtaining an actuator whose rotor (or ‘mover’) can perform both motions simultaneously. As an additional feature, a LiRA can be equipped with Magnetic Bearings (MBs) instead of conventional mechanical bearings, which due to their non-contact nature do not experience mechanical wear, offering extended lifetime and allowing operation in special high-purity environments. The MBs can also be integrated into the actuator in different ways [3], obtaining a compact *Self-Bearing* (SB) machine. It has to be noticed, however, that MBs are inherently unstable and require fast and accurate feedback control of the magnetically levitated mover’s position. Examples of SB machines with a Double-Stator (DS) configuration have been reported e.g. in [4], together with their control system. However, such machines can only perform rotary motion. The SB DS LiRA of **Fig. 1 (a)** has been proposed in [5] and its machine design and geometry optimization have been thoroughly discussed. The aim of this paper is to present its control-oriented modeling and analysis, with all the steps required to bring it into operation, i.e. to achieve simultaneous control of MBs and linear-rotary motion. This challenging task requires fast execution of multiple cascaded position and stator current control loops, together with Field Oriented Control (FOC). This paper is structured as follows. **Sec. II** describes briefly the topology of the proposed SB DS LiRA, with an insight on force/torque generation, MBs integration and the required number of phase currents to supply, finally leading to a control overview of the full system. In **Sec. III**, the non-linear electromechanical model of the SB DS LiRA is derived analytically and then linearized and analyzed in **Sec. IV**, defining the bandwidth requirements for cascaded feedback control. In **Sec. V**, details on the realized hardware prototype are provided, with focus on the implementation challenges of the embedded digital controller. Finally, **Sec. VI** presents and discusses the experimental measurements demonstrating full operation of the system and **Sec. VII** concludes the paper.

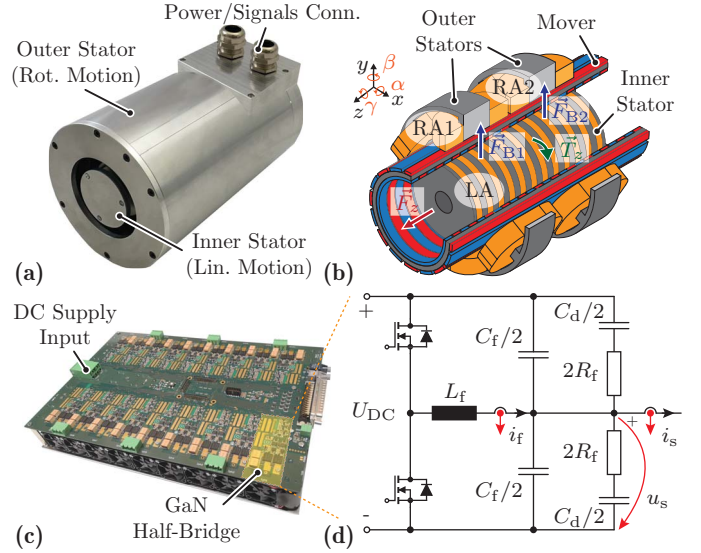


**Fig. 1:** (a) Realized hardware prototype of the SB DS LiRA, with inner and outer stators assembled. (b) Topology of the proposed SB DS LiRA with the generated electromechanical forces and torques. (c) 18-phase GaN DS LiRA inverter prototype. It is supplied with a single  $U_{DC} = 400$  V input and features 6 $\times$ 3 LC-filtered phase outputs. (d) Schematic of a single half-bridge of the DS LiRA inverter with symmetric damped LC output filter referred to DC+ and DC-. The component values are reported in **Tab. I**.

## II. OVERVIEW OF THE SB DS LiRA SYSTEM

During operation, the mover of the SB DS LiRA has to be completely supported magnetically. Mechanically, this means that its position  $(x, y, z)$  and orientation  $(\alpha, \beta, \gamma)$  with respect to a fixed inertial reference frame have to be controlled, i.e. a total of 6 Degrees of Freedom (DoF). In order to achieve this, at least 6 independent electromechanical forces and torques have to be generated by the stator, i.e. one per each DoF to control. This requires a specific machine topology and winding arrangement, for which many different alternatives exist [3].

### A. Proposed Actuator Topology

As shown in **Fig. 1 (b)**, the proposed actuator features a DS topology consisting of an inner and an outer stator interacting with two sets of Permanent Magnets (PMs) on the inner and outer surfaces of the mover, respectively. The inner stator hosts the Linear Actuator (LA) part of the machine, providing the linear driving force  $\vec{F}_z$ . The Rotary Actuator (RA) is located in the outer stator and provides the driving torque  $\vec{T}_z$ . As described in the following subsection, the MBs are beneficially integrated in the RA. Importantly, in order to control the tilting of the mover (i.e. the angles  $\alpha$  and  $\beta$ ), the RA is divided into two identical, axially displaced RAs, providing two distinct bearing forces  $\vec{F}_{B1}$  and  $\vec{F}_{B2}$ . In contrast to the LA, which as traditional linear machines requires only 3 phase currents to operate, 6 distinct phase currents are supplied to the coils of each RA.

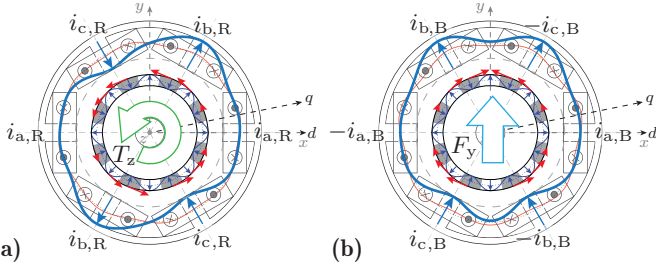


**Fig. 2:** Diagrams of the RA for (a) driving torque and (b) bearing force generation, for the special case with RA electrical mover angle  $\varphi = 0$ . The three-phase currents are  $i_{a,\{R,B\}} = \hat{I}_{\{R,B\}} \cos(\varphi_{s,\{R,B\}})$ ,  $i_{b,\{R,B\}} = \hat{I}_{\{R,B\}} \cos(\varphi_{s,\{R,B\}} + \frac{2\pi}{3})$  and  $i_{c,\{R,B\}} = \hat{I}_{\{R,B\}} \cos(\varphi_{s,\{R,B\}} + \frac{4\pi}{3})$  with  $\varphi_{s,\{R,B\}}$  the angle of the rotary/bearing stator field distributions. The angle  $\varphi_{\{R,B\}} = \varphi_{s,\{R,B\}} - \varphi$  is the relative angle between stator and rotor distributions. For both diagrams,  $\varphi_{\{R,B\}} = 90^\circ$ . The stator field distributions are obtained by integrating the total current loading and considering only the first 10 harmonics.

### B. RA with Combined Winding: Simultaneous Driving Torque and Bearing Force Generation

In order to explain how MBs are integrated in the RA and why 6 phase currents are used, consider the diagrams of **Fig. 2**. It is known that given a rotor field distribution with  $P$  pole pairs, a stator field distribution with the same number  $p$  of pole pairs has to be generated in order to provide torque, whereas a stator field distribution with  $p \pm 1$  pole pairs enables magnetic levitation [6]. In the considered case with 6 slots and *tooth concentrated windings*, a mover with e.g  $p = 4$  or  $p = 8$  could be used for simultaneous torque and bearing force generation. In order to use smaller PMs,  $p = 8$  is selected, which also reduces the thickness of the mover's back-iron without risk of saturations, and hence the mass to be levitated. With the employed winding arrangement, it is possible to combine both  $P$  and  $P \pm 1$  stator field distributions by superimposing the currents needed for torque and bearing force generation. In particular, the three-phase currents responsible for torque generation  $i_{\{a,b,c\},R}$  have to be impressed in the six coils of the RA as shown in **Fig. 2 (a)**. This way, the generated stator field distribution exhibits an harmonic component with  $p = 8$  pole pairs along the circumferential direction. As it can be observed, torque is generated when the relative (electrical) angle between the stator and rotor field distributions is  $\varphi_R = 90^\circ$ , as for traditional synchronous machines with surface PMs and non-salient rotor. To generate radial bearing forces, the three-phase currents  $i_{\{a,b,c\},B}$  are instead alternated as shown in **Fig. 2 (b)**. With this arrangement, the resulting field distribution exhibits an harmonic component with  $p - 1 = 7$  pole pairs. This time, in the case with a relative angle  $\varphi_B = 90^\circ$  a net bearing force along the  $y$ -direction is generated, whereas for  $\varphi_B = 0^\circ$  the net force points towards the  $x$ -direction.

Therefore, the total currents to impress for the RA are finally

$$\begin{bmatrix} i_1 \\ i_2 \\ i_3 \\ i_4 \\ i_5 \\ i_6 \end{bmatrix} = \begin{bmatrix} i_{a,R} + i_{a,B} \\ i_{b,R} - i_{c,B} \\ i_{c,R} + i_{b,B} \\ i_{a,R} - i_{a,B} \\ i_{b,R} + i_{c,B} \\ i_{c,R} - i_{b,B} \end{bmatrix} = \underbrace{\begin{bmatrix} 1 & 0 & 0 & 1 & 0 & 0 \\ 0 & 1 & 0 & 0 & 0 & -1 \\ 0 & 0 & 1 & 0 & 1 & 0 \\ 1 & 0 & 0 & -1 & 0 & 0 \\ 0 & 1 & 0 & 1 & 0 & 1 \\ 0 & 0 & 1 & 1 & -1 & 0 \end{bmatrix}}_{\mathbf{W}} \begin{bmatrix} i_{a,R} \\ i_{b,R} \\ i_{c,R} \\ i_{a,B} \\ i_{b,B} \\ i_{c,B} \end{bmatrix} \quad (1)$$

with the superposition matrix  $\mathbf{W}$ . The three-phase currents responsible for bearing force generation can be seen as a differential component on top of the ones responsible for driving torque generation, as they are added in one case and subtracted in the other.

The diagrams of **Fig. 2** are shown only for the case with the electrical mover angle  $\varphi = 0$ . It can be verified that simultaneous torque and bearing force generation are also guaranteed for  $\varphi \neq 0$ , provided that the currents are adjusted accordingly. In other words, by *orienting the field* (FOC) to the mover's ( $dq$ ) reference frame, the considerations presented so far can be generalized, derived analytically as in [7] and expressed with the following equations for the torque

$$T_{z\{1,2\}} = K_R i_{q,R\{1,2\}}; \quad T_z = T_{z1} + T_{z2} \quad (2)$$

and the radial bearing forces

$$\begin{bmatrix} F_{x\{1,2\}} \\ F_{y\{1,2\}} \end{bmatrix} = K_B \begin{bmatrix} i_{d,B\{1,2\}} \\ i_{q,B\{1,2\}} \end{bmatrix} \quad (3)$$

where  $K_R$  and  $K_B$  are respectively the torque and bearing machine constants of the SB DS LiRA. Analogously and for completeness, with FOC the LA generates the axial driving force

$$F_z = K_L i_{q,L} \quad (4)$$

with  $K_L$  the linear machine constant.

### C. Power Supply: 15 Half-Bridges with LC Filtered Output Voltage

With 6 phase currents per RA and 3 phase currents for the LA, a total of 15 phase currents have to be supplied. Such currents are generated by the same number of half-bridges of the DS LiRA inverter **Fig. 1 (c)**, each having the schematic of **Fig. 1 (d)**. The damped LC filter is added at the output of the half-bridge in order to supply the machine with smooth voltages. This reduces the emission of electromagnetic interference and prevents unwanted noise resulting from the rapidly changing switching voltage  $u_{sw}$  from affecting particularly the digital lines of the position sensors. In this case, in order to guarantee high dynamics, not only the output stator currents  $i_s$  are controlled, but also each intermediate stage of the filter, i.e. the output voltages  $u_s$  and the inductor currents  $i_f$ .

### D. Cascaded Control Structure

At this point the overall control structure for the SB DS LiRA can be described with the block diagram of **Fig. 3**. The outer control loop of the cascaded structure is the position control loop, where the MBs control the radial, the RA the rotary and the LA the linear position. It would be possible to design a complete multi-input-multi-output (MIMO) Center of Gravity (CoG) position controller for the DS LiRA [8]. However, given the complicated structure of the overall system and the stringent computation time requirements (cf. **Sec. V**), a *decentralized control strategy* is used. This consists in controlling the radial positions  $x_{\{1,2\}}$  and  $y_{\{1,2\}}$  independently with the corresponding RA stator (cf **Fig. 4**). Linear and rotary positions  $z$  and  $\gamma$  are also adjusted by independent controllers. This way, a collection of 6 simple SISO PID position controllers can be used, as many as the DoF to be controlled. The position controllers command the required forces and torques to be generated. As previously shown in **Sec. II-B**, these can be directly converted with the machine constants into references for the corresponding  $dq$  currents, adjusted by the inner  $dq$  stator current control loop of **Fig. 3**.

The outputs of the  $dq$  stator current controllers are the reference  $dq$  voltages to be applied to the winding of the DS LiRA. In order to be correctly generated by the inverter, it is first necessary to transform them back to phase voltages and combine the three-phase systems for torque and bearing forces generation with the superposition matrix  $\mathbf{W}$ . The inverter drives the *electrical system*, which is derived in **Sec. III-A** and describes the transient behavior of the stator currents

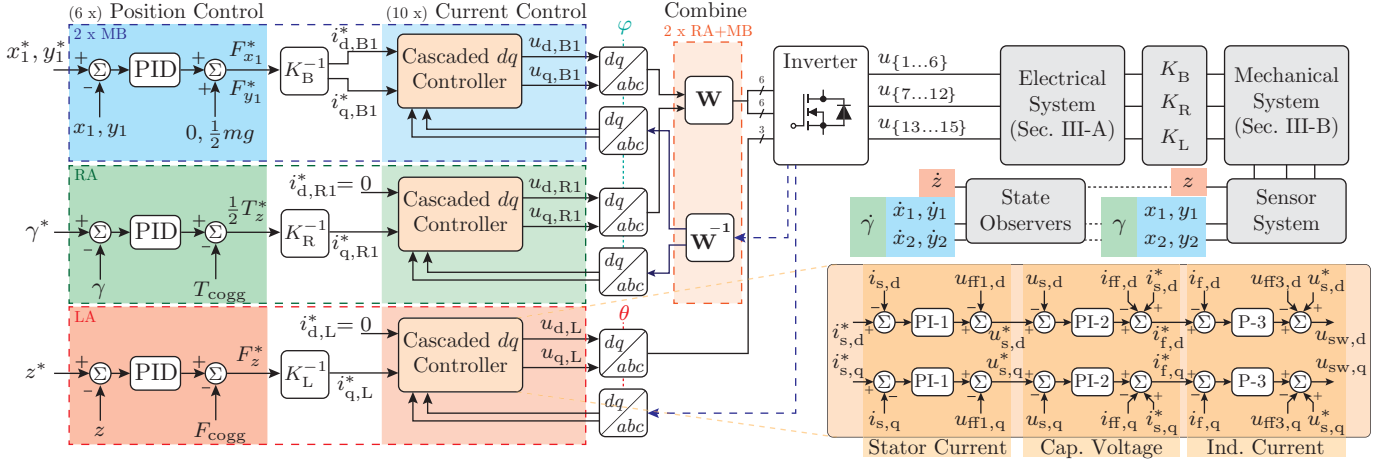


**Fig. 3:** Overview of the 6 DoF cascaded DS LiRA position controller. For the outer loop, a decentralized position control strategy is used, i.e. each of the positions  $x_{\{1,2\}}$ ,  $y_{\{1,2\}}$ ,  $z$ ,  $\gamma$  is controlled by an independent PID controller. The following feedforward compensations are applied: gravity force on the  $y_{\{1,2\}}$  controllers and cogging force and torque  $F_{\text{cog}}$  and  $T_{\text{cog}}$  on  $z$  and  $\gamma$  controllers. As these components are known disturbances, they are precomputed and improve the controller's reaction. The inner  $dq$  stator current controllers also consists of multiple cascaded loops (stator current, capacitor voltage, inductor current), shown in detail in the orange box. In this case the feedforward components ensure correct decoupling of the  $d$  and  $q$  channels, as well as compensation of the induced voltages. All the measured phase quantities  $i_f$ ,  $u_s$  and  $i_s$  are transformed into  $dq$  with the appropriate electrical angle.

in the coils of the RA or the LA. In turn, these generate the electromechanical forces and torques which are the inputs of the *mechanical system*, derived in **Sec. III-B** and describes the transient behavior of the mover's position and orientation.

In order to close the control loops, it is necessary to measure all the quantities to be controlled. The sensor system of the DS LiRA provides a total of 52 measurements, of which  $15 \times 3$  are the electrical quantities  $i_f$ ,  $u$  and  $i$  of the half bridges with output filter, one is the DC-Link voltage  $U_{\text{DC}}$  and 6 are the positions  $x_{\{1,2\}}$ ,  $y_{\{1,2\}}$ ,  $z$  and  $\gamma$ . As it will be explained in **Sec. IV-B**, the position measurements are fed to the same number of state observers to also get smooth estimates of the velocities, used for improved derivative control.

### III. ELECTROMECHANICAL SYSTEM MODEL

As a next step, all the aforementioned dynamical models need to be derived. With these it is possible to simulate the full behavior of the DS LiRA system and to design each current or position controller and the desired state observers.

#### A. Electrical System Modeling

As mentioned, the model of the electrical system describes the transient behavior of each phase current. Also the dynamics of the LC output filter is modeled in this section. For the  $i$ -th half-bridge with the schematic of **Fig. 1 (d)**, by simple circuit analysis one can model the filter inductor current  $i_f$  as

$$u_{\text{sw},i} = L_f \frac{di_{f,i}}{dt} + u_{s,i}, \quad (5)$$

the output voltage at the filter capacitor  $u_{s,i}$  (neglecting the damping elements in parallel, as the impedance of  $C_d$  dominates over  $R_d$ ) as

$$i_{f,i} = \underbrace{(C_f + C_d)}_{2C_f} \frac{du_{s,i}}{dt} + i_{s,i}, \quad (6)$$

and the output stator current  $i_{s,i}$  with the *stator equation*

$$u_{s,i} = R_i i_{s,i} + L_i \frac{di_{s,i}}{dt} + \frac{d\psi_i}{dt}, \quad (7)$$

where the term  $\frac{d\psi_i}{dt}$  is the induced voltage in the  $i$ -th stator coil caused by the changing flux linkage of the mover's PMs due to linear, rotary or radial motion. This is the main coupling element between the

electrical and mechanical subsystems, which is effectively countered by using cascaded control. Although the values of  $L_f$  and  $C_f$  are the same for all half bridges,  $R_i$  and  $L_i$  are different for RA and LA, according to the connected stator coil. The half-bridges 1 to 6 are used for the RA1, 7 to 12 for the RA2 and 13 to 15 for the LA, hence

$$(R_i, L_i) = \begin{cases} (R_{\text{rot}}, L_{\text{rot}}) & \text{for } i = \{1, \dots, 12\} \\ (R_{\text{lin}}, L_{\text{lin}}) & \text{for } i = \{13, \dots, 15\} \end{cases} \quad (8)$$

As discussed in **Sec. II-B**, the necessary electromechanical forces and torques are generated by the corresponding field-oriented controlled three-phase systems. There are 5 of them in total: two per RA, which are then superimposed (indicated in the following with R1, B1, R2, B2), and one for the LA (indicated with L). For each case, the field has to be oriented according to the electrical angle

$$\vartheta = \begin{cases} \varphi = P\gamma & \text{for the outer PMs (R1, B1, R2, B2)} \\ \theta = \frac{2\pi}{\tau_{\text{pp}}} z & \text{for the inner PMs (L)} \end{cases} \quad (9)$$

where  $\tau_{\text{pp}}$  is the pole pitch of the inner PM array. By applying the  $dq$  transformation (function of  $\vartheta$ ) to (5), (6) and (7), it can be verified that the dynamic equations in the field-oriented  $dq$  mover frame for each three-phase system  $\{R1, B1, R2, B2, L\}$  are:

$$u_{\text{sw},\{d,q\}} = L_f \frac{di_{f,\{d,q\}}}{dt} \mp L_f \underbrace{\frac{d\vartheta}{dt} i_{f,\{q,d\}}}_{u_{\text{ff1},\{d,q\}}} + u_{s,\{d,q\}}, \quad (10)$$

$$i_{f,\{d,q\}} = 2C_f \frac{du_{s,\{d,q\}}}{dt} \mp 2C_f \underbrace{\frac{d\vartheta}{dt} i_{f,\{q,d\}}}_{i_{\text{ff},\{d,q\}}} + i_{s,\{d,q\}}, \quad (11)$$

and

$$u_{s,\{d,q\}} = R_{\{d,q\}} i_{s,\{d,q\}} + L_{\{d,q\}} \frac{di_{s,\{d,q\}}}{dt} + \underbrace{-\frac{d\vartheta}{dt} L_{\{d,q\}} i_{s,\{q,d\}} + \frac{d\psi_{\{d,q\}}}{dt} - \frac{d\vartheta}{dt} \psi_{\{q,d\}}}_{u_{\text{ff3},\{d,q\}}}. \quad (12)$$

Due to the machine's symmetry (non-salient pole rotor)

$$(R_d, L_d) = (R_q, L_q) = \begin{cases} (R_{\text{rot}}, L_{\text{rot}}) & \text{for R1, B2, R2, B2} \\ (R_{\text{lin}}, L_{\text{lin}}) & \text{for L} \end{cases} \quad (13)$$

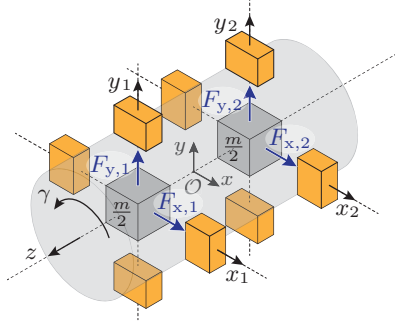


**Fig. 4:** Diagram of the mover as a rigid body showing the decentralized control strategy used for MBs. Instead of controlling the position and orientation of the Center of Gravity  $\mathcal{O}$ , the radial positions  $x_{\{1,2\}}$  and  $y_{\{1,2\}}$  are controlled independently by the bearing forces generated with the respective RA.

It is important to note the cross-coupling terms appearing in the  $dq$  dynamic equations as a result of the  $dq$ -transformation of the time derivatives. These terms have to be compensated (typically in feedforward) in order to ensure correctly decoupled  $dq$  control. For the flux linkage it holds

$$(\psi_d, \psi_q) = \begin{cases} (\hat{\Psi}_{PM,lin}, 0) & \text{for L} \\ (\hat{\Psi}_{PM,rot}, 0) & \text{for R1, R2} \\ (\hat{\Psi}_{PM,mb} x, \hat{\Psi}_{PM,mb} y) & \text{for B1, B2} \end{cases} \quad (14)$$

### B. Mechanical System Modeling

The mechanical dynamics of the mover is usually described by its Equations of Motion (EoM), which relate the position and orientation of the rigid body to the applied forces and torques. These are derived by defining a set of generalized coordinates to be used in the *Lagrange* or *Newton-Euler* equations. By considering the full position and orientation of the mover and describing the dynamics in terms of its CoG coordinates, it is possible to derive a complete multi-variable mechanical model, which also considers the cross-couplings between the different modes of the system [6] [8]. In this case however, for decentralized control it is sufficient to derive the following 6 independent mechanical subsystems (cf. **Fig. 4**):

$$\frac{d^2 x_{\{1,2\}}}{dt^2} = \frac{2}{m} (F_{x_{\{1,2\}}} + F_{pull,x_{\{1,2\}}}) \quad (15)$$

$$\frac{d^2 y_{\{1,2\}}}{dt^2} = \frac{2}{m} (F_{y_{\{1,2\}}} + F_{pull,y_{\{1,2\}}} + F_g) \quad (16)$$

$$\frac{d^2 z}{dt^2} = \frac{1}{m} (F_z + F_{cogg}) \quad (17)$$

$$\frac{d^2 \gamma}{dt^2} = \frac{1}{J} (T_z + T_{cogg}) \quad (18)$$

where

- each radial subsystem is assumed to support half of the mover mass  $\frac{m}{2}$ . This assumption is valid as long as the mover is not axially displaced too far away from the center;
- the radial pull forces  $F_{pull,x_{\{1,2\}}} = K_{pull,x_{\{1,2\}}} \cdot x_{\{1,2\}}$  and  $F_{pull,y_{\{1,2\}}} = K_{pull,y_{\{1,2\}}} \cdot y_{\{1,2\}}$  model the magnetic attraction existing between the mover's PMs and the stators' iron cores. Due to the symmetry of the actuator,  $K_{pull,x_{\{1,2\}}} = K_{pull,y_{\{1,2\}}} = K_{pull}$  and the net radial pull forces are zero if the mover is perfectly in the center of the machine;
- the gravity force is  $F_g = -\frac{m}{2} g$  and acts along the  $y$  axis;
- the cogging force depends on the axial position  $z$  and is modeled as  $F_{cogg}(z) = -\hat{F}_{cogg} \sin(2\theta) = -\hat{F}_{cogg} \sin(\frac{4\pi}{\tau_{pp}} z)$ , whereas the cogging torque is, analogously,  $T_{cogg} = -\hat{T}_{cogg} \sin(6\varphi)$ .

## IV. MODEL LINEARIZATION AND CONTROLLER DESIGN

In order to design the position controllers, the dynamics of each subsystem is linearized around a certain *steady-state* (ss) equilibrium point. These can be found by equating the right-hand terms of (15) to (18) to zero. For the radial dynamics  $x_{ss,\{1,2\}} = 0$  and  $y_{ss,\{1,2\}} = 0$  are chosen, as normally the mover's radial position is controlled to the center of the actuator. The corresponding steady-state inputs for which the equilibrium condition is satisfied are  $F_{x,ss,\{1,2\}} = 0$  and the gravity compensations  $F_{y,ss,\{1,2\}} = -F_g$ , which are provided as feedforward components (cf. **Fig. 3**). As the derived models (15) and (16) are already linear, one can directly write the transfer functions

$$G_{\{x,y\}_{\{1,2\}}}(s) = \frac{\{X, Y\}_{\{1,2\}}(s)}{F_{\{x,y\}_{\{1,2\}}}(s)} = \frac{1}{\frac{m}{2} s^2 - K_{pull}} \quad (19)$$

where  $s$  is the Laplace variable. The poles of (19) are

$$\lambda_{\{x,y\}\pm} = \pm \sqrt{2K_{pull}/m} \quad (20)$$

i.e. the radial dynamics is unstable, as all the subsystems show a right-half-plane pole. For the axial dynamics, it has to be considered that the axial position  $z$  varies in an entire range of operating points  $z_{ss} \in [z_{min}, z_{max}]$ , to which the steady-state input  $F_{z,ss} = -F_{cogg}(z_{ss})$  corresponds. Due to the non-linear dependency of  $F_{cogg}$  on  $z$ , the stability of the linearized  $z$  dynamics depends on the considered  $z_{ss}$ . This can be seen by linearizing (17) with  $z_{ss}$  as a parameter, obtaining the transfer function

$$G_z(s, z_{ss}) = \frac{Z(s)}{F_z(s)} = \frac{1}{m s^2 + \hat{F}_{cogg} \cos\left(\frac{4\pi}{\tau_{pp}} z_{ss}\right)} \quad (21)$$

which has the poles

$$\lambda_{z\pm}(z_{ss}) = \pm j \sqrt{\hat{F}_{cogg} \cos\left(\frac{4\pi}{\tau_{pp}} z_{ss}\right) / m} \quad (22)$$

where  $j = \sqrt{-1}$  is the imaginary unit. For a linearly increasing  $z_{ss}$ , the poles leave the imaginary axis and one of them enters the right half-plane. Therefore, the axial position controller can be designed for the worst-case instability (i.e. when the unstable pole has the largest real part), which is obtained for  $z_{ss} = \frac{\tau_{pp}}{4}$ . The same considerations apply to the rotational dynamics.

For the stator current control, it can be observed that all the  $dq$  models derived in **Sec. III-A** are already linear and stable, so they can be directly used for controller design as in **Fig. 3**. In order to compensate for the output LC filter dynamics, the classical inner-loop stator current control is extended with two additional nested control loops for the capacitor voltage  $u$  and the inductor current  $i_f$ . Differently from (6), the transfer function used for capacitor voltage control also considers the damping elements.

### A. Bandwidth Requirements and Separation of Loop Dynamics

The unstable poles in (20) and (22) set a lower bound on the bandwidth of the respective closed loop controllers, which needs to be approximately two times larger than the largest unstable pole [9]. In turn, in order to guarantee separation of the dynamics between the loops of the cascaded structure, the bandwidth of each inner controller has to be approximately 5 times larger than the very next outer loop.

With the parameters of the DS LiRA given in **Tab. I**, the largest unstable pole is  $\lambda = 748.1 \text{ rad s}^{-1} = 119 \text{ Hz}$ , which imposes a bandwidth of at least 240 Hz for the bearing position controller. Consequently, the bandwidths of the inner control loops are defined, with ideally 31.25 kHz for the innermost inductor current controller. Nevertheless, also the switching frequency of the power electronics

**TABLE I:** Parameters of the DS-LiRA.

Symbol	Quantity	Value
<b>Machine Constants</b>		
$K_L$	Force Const.	83.5 N A <sup>-1</sup>
$K_R$	Torque Const. per RA	0.21 N m A <sup>-1</sup>
$K_B$	Bearing Const. per RA	3.7 N A <sup>-1</sup>
$K_{pull}$	Attraction Const. per RA	375 N mm <sup>-1</sup>
<b>Mechanical Parameters</b>		
$m$	Mover Mass	1.34 kg
$J$	Mover $z$ -Axis Mol	0.001 45 kg m <sup>2</sup>
$\tau_{PP}$	Pole Pitch of Inner PM array	12.5 mm
$\hat{F}_{cog}$	Max Cogging Force	20 N
$\hat{T}_{cog}$	Max Cogging Torque	0.0376 N m
<b>Electrical Parameters</b>		
$f_{sw}$	Switching Frequency	140 kHz
$R_{rot}$	Coil Resistance (RA)	1.8 $\Omega$
$L_{rot}$	Coil Inductance (RA)	2.4 mH
$R_{lin}$	Coil Resistance (LA)	6.3 $\Omega$
$L_{lin}$	Coil Inductance (LA)	31 mH
$L_f$	Filter Inductance	80 $\mu$ H
$C_f = C_d$	Filter Capacitance	4.8 $\mu$ F
$R_f$	Damping Resistance	6.8 $\Omega$
$\hat{\Psi}_{PM,rot}$	Peak PM Flux Linkage (RA)	20.7 mWb
$\hat{\Psi}_{PM,lin}$	Peak PM Flux Linkage (LA)	110 mWb

supply  $f_{sw} = 140$  kHz has to be considered. This imposes an upper bound on the achievable inductor current control bandwidth, which is ideally around  $0.1 f_{sw} = 14$  kHz, for the considered case. For this reason, the separation factors between the loops of the cascaded stator current controller are smaller than 5, as it can be seen from the chosen bandwidths of **Tab. II**, with the highest bandwidth of 21 kHz slightly exceeding the ideal upper bound.

### B. PID Position Controllers with State Observers

The PID controllers used for position control are tuned according to the gains of **Tab. II**. As usual, integral action is needed to suppress steady-state errors due to unmodeled disturbances, thus allowing precise positioning in the  $\mu$ m range, a limit given by the available sensor resolution. As anti-windup scheme, the integration is stopped when the output is above its saturation limits, also reported in **Tab. II**. Furthermore, it can be shown that derivative action is necessary in order to stabilize the second order dynamics of the mechanical subsystems. As the numeric calculation of the error derivative is prone to noise, smooth estimates provided by Luenberger state observers are used instead. The used values for the observer gain matrix  $L_{obs} = \text{diag}(l_{11}, l_{22})$  are reported in **Tab. II**.

## V. HARDWARE REALIZATION AND DIGITAL CONTROLLER IMPLEMENTATION

The realized prototype of the SB DS LiRA is shown in **Fig. 1 (a)**. Further details about its construction and physical dimensions, also for the DS LiRA inverter of **Fig. 1 (b)**, can be found in [5].

**TABLE II:** Chosen controller gains and bandwidths

Bearing Contr.		Rotary Contr.		Linear Contr.	
$k_P$	680 N/mm	25 N m/rad	125 N/mm		
$k_I$	10200 N/(mm s)	99 N m/(rad s)	5862 N/(mm s)		
$k_D$	2.55 N s/(mm)	0.8 N m s/(rad)	1 N s/(mm)		
Sat.	$\pm 26.2$ N	$\pm 0.839$ N m	$\pm 166$ N		
$l_{11}$	0.06	1	0.02		
$l_{22}$	0.04	0.005	0.09		
$f_{BW}$	625 Hz	137 Hz	93 Hz		
Stator Current		Capacitor Voltage		Inductor Current	
$k_P$	40 V/A	0.405 V/A	10.23 V/A		
$k_I$	20000 V/(A s)	3553 V/(A s)	0 V/(A s)		
$f_{BW}$	2.60 kHz	8.37 kHz	20.9 kHz		

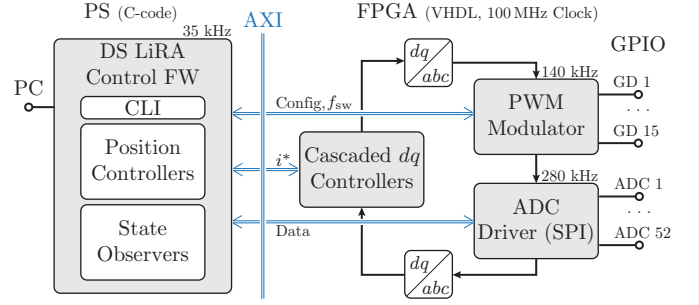


**Fig. 5:** Block diagram of the DS LiRA control algorithm, implemented both in the PS (in C-code) and the FPGA (in VHDL) of the *Xilinx Zynq-7020*. The  $dq$  transformations and the cascaded  $dq$  stator current control loops are implemented in the FPGA. The commanded  $dq$  switching voltages are transformed into phase quantities and assigned as duty cycles to the PWM Modulator, which finally provides the Gate Drive (GD) signals to the power switches. The PS provides configuration values and controller setpoints by accessing the registers via AXI protocol. It finally communicates with a computer via UART through a Command Line Interface (CLI).

The presented control structure is implemented on a processing module. The *Trenz TE0720* System-on-Module (SoM) with a *Xilinx Zynq-7020* System-on-Chip (SoC) is used. The module is hosted on the DS LiRA inverter and includes all power supplies and required external components to operate the SoC, allowing for fast electronic design process. The control algorithm is implemented both in the Processing System (PS) and the Field Programmable Gate Array (FPGA) of the SoC, as illustrated in **Fig. 5**. The main bottleneck of the module is the access time required to read a single 32-bit register with the PS using AXI Lite protocol, which is about 250 ns. The execution time of the digital controller is important, as in order to minimize the effect of discretization the sampling frequency is typically selected a factor of 10 above the largest controller bandwidth. The large number of measurements,  $dq$  transformations and PID controllers to be executed make it challenging to meet the bandwidth requirements in the hardware. For this reason, all the computations needed for the (faster) inner stator current control loops (including capacitor voltage and inductor current) are moved to the FPGA. The control firmware in the PS assigns the  $dq$  stator current references, which are obtained from the position controllers. These can be executed at 35 kHz, together with the state observers and the main communication interface.

## VI. EXPERIMENTAL RESULTS

In *this* section the proposed and implemented control system is verified with experimental measurements on the DS LiRA prototype.

### A. Cascaded Stator Current Control

The stator current controller is verified with the step response of **Fig. 6**. A  $d$ -component stator current step of 3 A in one RA subsystem is shown, both from simulations and measurements. The  $q$ -component is not shown as it is successfully controlled to zero. Moreover, the two components are decoupled, also due to constant electrical angle  $\varphi = 0$  assumed. With the approximation

$$f_{BW} \approx \frac{1}{3 \cdot t_{rise}} = \frac{1}{3 \cdot 0.12 \text{ ms}} = 2.78 \text{ kHz} \quad (23)$$

the achievable stator current controller bandwidth is estimated from the 10% to 90% rise time  $t_{rise}$  and it corresponds to the designed bandwidth of 2.6 kHz (cf. **Tab. II**). The stator current control loop commands the reference to the next inner loop, i.e. the capacitor voltage controller, with the shown response. It can be observed that

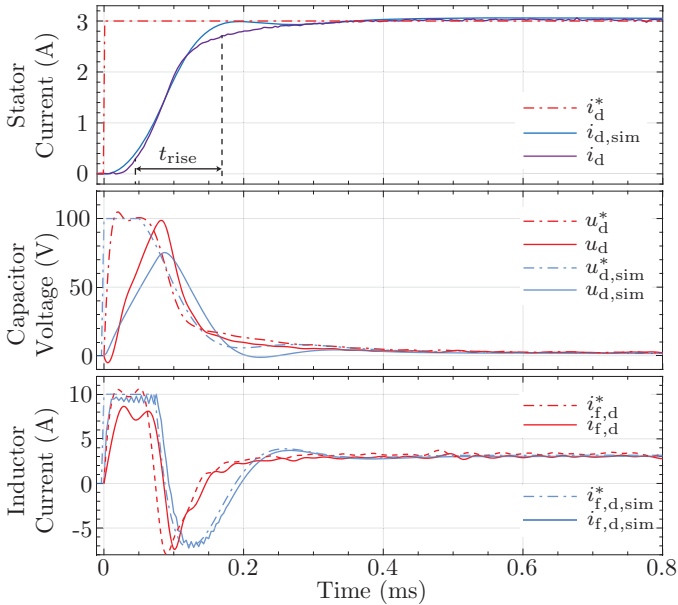


**Fig. 6:** Measured and simulated (MATLAB Simulink) response of the cascaded  $dq$  stator current controller for  $U_{DC} = 200$  V operation. A step of 3 A is commanded to the  $d$ -component of one RA subsystem, whereas the  $q$ -component is controlled to zero and hence not shown. With a rise time of about  $t_{rise} = 0.12$  ms, a bandwidth of 2.78 kHz is estimated.

the capacitance in simulation is slightly higher than the effective capacitance present on the hardware. Finally, it can also be observed that the innermost inductor current controller saturates during charging of the filter capacitor.

### B. Simultaneous Levitation and Linear-Rotary Motion Control

To show full operation of the SB DS LiRA, a mission profile with a start-up phase, simultaneous linear-rotary steps and shutdown is shown in **Fig. 7**. The mover is kept at rest close to the center of the machine with auxiliary teflon touchdown bearings. This allows to reduce the large currents required for lift-off. During the first seconds, the mover is turned to  $\gamma = 0^\circ$ , and driven in the positive  $z$ -direction to exit the touchdown bearings and start to levitate. When the MBs are stable in the center position, i.e. when all radial positions are below  $\pm 20 \mu\text{m}$  for 250 ms, the active phase starts. The mover tracks the stepping reference between the two positions ( $\gamma_1 = 0^\circ, z_1 = 8$  mm) and ( $\gamma_2 = 80^\circ, z_2 = 14$  mm). It can be clearly seen that the measured radial positions also step between two positions up to  $55 \mu\text{m}$  apart, although they should be controlled to zero. This depends on many different factors, like e.g. the irregular external surface of the mover or the uneven magnetization of its PMs. Last but not least, as mentioned the implemented SISO controller does not consider the existing couplings between linear and radial motions. The last two seconds show the shutdown procedure, where the rotational position is kept constant and the linear position is decreased at a constant velocity of  $10 \text{ mm s}^{-1}$  until the mover is again fixed in the touchdown bearings. When  $z = 2.7$  mm, the bearing controller is stopped and the mover moves back to the initial position at  $z = 0$  mm.

## VII. CONCLUSION

In this paper the control-oriented modeling of a SB DS LiRA was presented and used to design a cascaded 6 DoF position controller. The experimental results on the realized prototype show successful operation of the actuator with simultaneous levitation and linear-rotary motion control. Future work includes improvement of the radial position controller in order to suppress disturbances. In this direction,

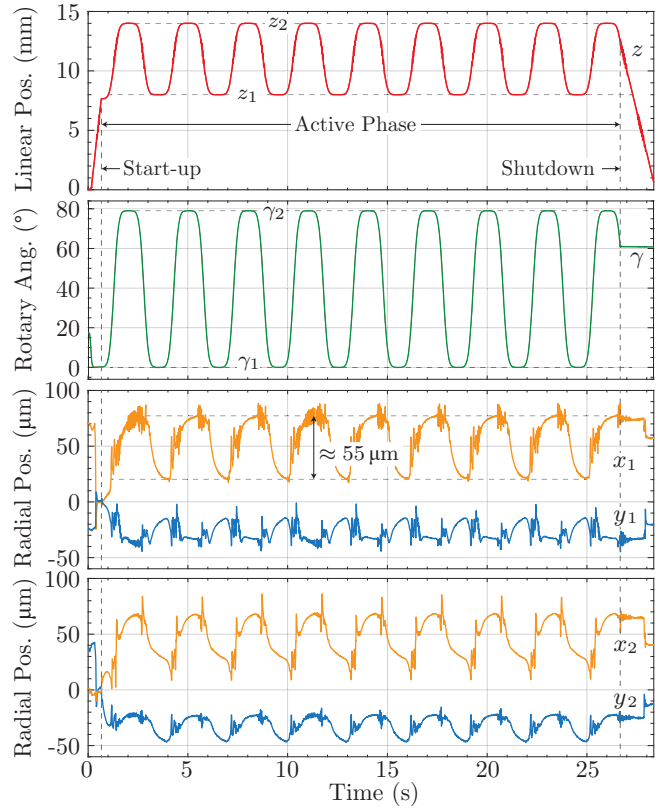


**Fig. 7:** Simultaneous levitation and linear-rotary motion control of the SB DS LiRA. Linear and rotary responses track very closely their references, whereas the radial positions only slightly deviate from the desired zero position.

an investigation on the potential benefits of a MIMO controller and its feasibility will be conducted.

## REFERENCES

- [1] T. Overboom, J. Jansen, E. Lomonova, and F. Tacken, "Design and Optimization of a Rotary Actuator for a Two-Degree-of-Freedom  $z - \varphi$  Module," *IEEE Transactions on Industry Applications*, vol. 46, no. 6, pp. 2401–2409, 2010.
- [2] A. Turner, K. Ramsay, R. Clark, and D. Howe, "Direct-Drive Rotary-Linear Electromechanical Actuation System for Control of Gearshifts in Automated Transmissions," *Proc. of IEEE Vehicle Power and Propulsion Conference*, pp. 267–272, 2007.
- [3] S. Mirić, D. Bortis, and J. W. Kolar, "Design and Comparison of Permanent Magnet Self-Bearing Linear-Rotary Actuators," *Proc. of 12th International Symposium on Linear Drives for Industry Applications (LDIA)*, pp. 1–6, 2019.
- [4] W. Peng, F. Zhang, and J.-W. Ahn, "Design and Control of a Novel Bearingless SRM with Double Stator," *Proc. of 2012 IEEE International Symposium on Industrial Electronics*, pp. 1928–1933, 2012.
- [5] S. Mirić, R. Giuffrida, G. Rohner, D. Bortis, and J. W. Kolar, "Design and Experimental Analysis of a Selfbearing Double-Stator Linear-Rotary Actuator," *Proc. of 2021 IEEE International Electric Machines and Drives Conference (IEMDC)*, p. 8, 2021.
- [6] H. Bleuler, M. Cole, P. Keogh, R. Larssonneur, E. Maslen, Y. Okada, G. Schweitzer *et al.*, *Magnetic Bearings: Theory, Design, and Application to Rotating Machinery*. Springer Science & Business Media, 2009.
- [7] S. Mirić, R. Giuffrida, D. Bortis, and J. W. Kolar, "Enhanced Complex Space Vector Modeling and Control System Design of Multiphase Magnetically Levitated Rotary-Linear Machines," *IEEE Journal of Emerging and Selected Topics in Power Electronics*, vol. 8, no. 2, pp. 1833–1849, 2020.
- [8] S. Mirić, R. Giuffrida, D. Bortis, and J. W. Kolar, "Dynamic Electromechanical Model and Position Controller Design of a New High-Precision Self-Bearing Linear Actuator," *IEEE Transactions on Industrial Electronics*, pp. 1–1, 2020.
- [9] S. Skogestad and I. Postlethwaite, *Multivariable Feedback Control: Analysis and Design*, vol. 2. Wiley New York, 2007.